

Biohybrid microrobots locally and actively deliver drug-loaded nanoparticles to inhibit the progression of lung metastasis

Fangyu Zhang[†], Zhongyuan Guo[†], Zhengxing Li[†], Hao Luan, Yiyan Yu, Audrey T. Zhu, Shichao Ding, Weiwei Gao, Ronnie H. Fang, Liangfang Zhang*, Joseph Wang*

Lung metastasis poses a formidable challenge in the realm of cancer treatment, with conventional chemotherapy often falling short due to limited targeting and low accumulation in the lungs. Here, we show a microrobot approach using motile algae for localized delivery of drug-loaded nanoparticles to address lung metastasis challenges. The biohybrid microrobot [denoted “algae-NP(DOX)-robot”] combines green microalgae with red blood cell membrane-coated nanoparticles containing doxorubicin, a representative chemotherapeutic drug. Microalgae provide autonomous propulsion in the lungs, leveraging controlled drug release and enhanced drug dispersion to exert antimetastatic effects. Upon intratracheal administration, algae-NP(DOX)-robots efficiently transport their drug payload deep into the lungs while maintaining continuous motility. This strategy leads to rapid drug distribution, improved tissue accumulation, and prolonged retention compared to passive drug-loaded nanoparticles and free drug controls. In a melanoma lung metastasis model, algae-NP(DOX)-robots exhibit substantial improvement in therapeutic efficacy, reducing metastatic burden and extending survival compared to control groups.

INTRODUCTION

The lungs represent the most prominent target organ for cancer metastasis (1), occurring in 20 to 54% of patients diagnosed with malignant tumors that have metastasized (2). Systemic chemotherapy is a common approach for treating lung metastases (3); however, its effectiveness has been suboptimal due to poor lung accumulation and targeting issues (4). Now, there is no specific treatment tailored for lung metastasis (5). Recently, nanotechnology has emerged as a promising approach for improving the therapeutic outcomes of advanced metastatic malignancies (6). Nevertheless, the systemic administration of nanoparticles faces challenges from various biological barriers, often leading to the inefficiency of conventional nanoformulations in accumulating at metastatic sites (7–9).

The unique features and microenvironment of the lungs make them an attractive target for local drug delivery (10). For example, the large surface area of the alveoli is beneficial for rapid drug absorption (11) and prolonged drug deposition into the lungs (12). Extracellular enzyme levels for metabolic breakdown are minimal in the respiratory tract, thus enabling delivered payloads to avoid the first-pass metabolism that is characteristic of oral or intravenous administration routes (13). For the treatment of lung conditions, site-specific delivery enables high local concentrations to be achieved while reducing side effects on normal tissues caused by systemic exposure (14). While pulmonary delivery via inhalation or dry powder formulations has shown promise for treating pulmonary diseases (15–18), the rapid elimination of inhaled medications and limited delivery efficiency have constrained their therapeutic impact (7, 19). Consequently, developing highly efficient alternative pulmonary

delivery platforms is crucial to surpass current inhalation treatments and achieve more effective lung cancer treatment.

In recent years, extensive research efforts have been dedicated to leveraging microrobots for disease treatment (20–29). The autonomous movement on a small scale is one of the critical aspects of designing and building microrobots (30). Such active movement of drug-loaded microrobots holds the potential to enhance drug delivery efficiency and improve therapeutic efficacy. Compared to traditional passive drug delivery systems, microrobot-based active delivery exhibits appealing in vivo capabilities, such as transporting therapeutic payloads to target sites (31–33), penetrating tissue for enhanced retention, selectively positioning in the gastrointestinal tract (34–36), and accumulating and penetrating tumors (24, 26, 37). Special emphasis has been placed on the development of biohybrid microrobots, achieved by functionalizing unicellular microorganisms like algae, bacteria, sperm, etc., with synthetic components (24, 26, 38–40). Such biohybrid microrobots rely on the actuation capabilities of living microorganisms for powering and providing motion thrust for transporting synthetic payloads to accomplish various tasks (41–42). Among these microorganisms, algae have demonstrated considerable promise as motile biomotors in various biomedical and environmental applications (43). Microalgae-based robotic systems have distinct advantages, including sustained autonomous motility in localized environments, phototaxis, autofluorescence for imaging, and adaptability to different surroundings (36, 38, 44–48). Notably, algae-based microrobots offer notable benefits for the treatment of pulmonary diseases, including rapid dispersion and distribution throughout the lungs, prolonged retention, active drug delivery, and controlled drug release. These advantages have recently demonstrated remarkable antibacterial efficacy in combating pneumonia (29). The motion ability of the drug-loaded algae microrobots has resulted in a delayed lung clearance compared to static drug-loaded algae control, leading to enhanced bacterial reduction and significantly improved survival rates in mice compared

Copyright © 2024 The Authors, some rights reserved; exclusive licensee American Association for the Advancement of Science. No claim to original U.S. Government Works. Distributed under a Creative Commons Attribution NonCommercial License 4.0 (CC BY-NC).

Department of NanoEngineering and Chemical Engineering Program, University of California San Diego, La Jolla, CA 92093, USA.

*Corresponding author. Email: josephwang@ucsd.edu (J.W.); zhang@ucsd.edu (L.Z.)

†These authors contributed equally to this work.

to both the static control and passive drug-loaded nanocarrier control groups (29).

In this work, we design algae-based biohybrid microrobots for the active local delivery of chemotherapeutic drugs to combat melanoma lung metastasis (Fig. 1A). The microrobot platform [denoted “algae-NP(DOX)-robot”] consists of natural green algae functionalized with red blood cell (RBC) membrane-coated doxorubicin (DOX)-loaded polymeric poly(lactic-co-glycolic acid) (PLGA) nanoparticles for enhanced drug delivery to treat lung cancer. The prolonged swimming of microalgae facilitates the efficient distribution of therapeutics throughout the lungs, providing an effective strategy for addressing lung metastasis. Biodegradable PLGA nanoparticles play a crucial role in encapsulating anticancer drugs for controlled release, while the cell membrane coating imparts biomimetic properties that shield the therapeutic payload from the biological environment. These biohybrid microrobots, featuring functionalized microalgae, retain their attractive intrinsic motion capabilities even under physiological conditions, persisting seamlessly even after drug loading. Through intratracheal administration of algae-NP(DOX)-robots into the lungs of mice, we demonstrate their enhanced distribution and prolonged presence, resulting in a more effective accumulation of the loaded drugs. These findings align with the slow uptake of biohybrid robots by alveolar macrophages, which is likely a consequence of the unique motion capabilities of the microalgae carriers. Overall, there is a substantial improvement in therapeutic efficacy against melanoma lung metastasis, as evidenced by the reduced lung metastatic burden and substantially improved median survival time compared to passive drug-loaded nanoparticles and free drug controls.

RESULTS

Preparation of algae-NP(DOX)-robot

We first followed a well-established nanoprecipitation method to prepare DOX-loaded PLGA nanoparticles [denoted “PLGA(DOX)”] (49). A cell membrane coating was used to further shield the therapeutic agents. RBCs were chosen as the cell source for membrane coating due to their biocompatibility and ease of collection for scalable manufacturing (50). To create RBC membrane-coated DOX-loaded nanoparticles [denoted “NP(DOX)”), RBC membrane-derived vesicles were prepared and coated onto PLGA(DOX) through a sonication-based method (50). Transmission electron microscopy analysis confirmed the presence of a core-shell structure in NP(DOX) after the cell membrane coating (Fig. 1B). The final cell membrane-coated nanoparticles were relatively monodisperse, as illustrated by scanning electron microscopy (SEM) (fig. S1). Coating with the cell membrane increased the hydrodynamic diameter from 89.7 ± 1.3 nm to 108.1 ± 6.0 nm (Fig. 1C). In addition, the zeta potential of NP(DOX) was found to be -3 mV, in contrast to the $+35$ mV of PLGA(DOX), indicating that the cell membrane coating shielded the positively charged surface of PLGA(DOX) (Fig. 1D). The strong positive charge of PLGA(DOX) is attributed to the absorption of positively charged DOX molecules onto the negatively charged PLGA nanoparticles. After membrane coating, the negatively charged bilayer phospholipid membrane surface alters the surface charge of NP(DOX). A drug loading yield (DOX weight/PLGA weight) of 6.2 wt % was determined for PLGA(DOX), corresponding to a 24.8% encapsulation efficiency (DOX loading/DOX input); the loading yield of NP(DOX) decreased slightly to 5.6 wt %, indicating that that

the cell membrane coating had a minor impact on drug loading (Fig. 1, E and F).

To prepare algae-NP(DOX)-robots, we further conjugated NP(DOX) onto the surface of microalgae. We selected green algae, *Chlamydomonas reinhardtii*, to actuate our microrobot formulation due to its many attractive properties including effective and extended self-propulsion in biological media (29), versatile surface chemical groups (e.g., $-COOH$ and $-NH_2$) for cargo conjugation (44, 48), biocompatibility (51), autofluorescence for tracking and imaging (29), and recognition as safe for use by the US Food and Drug Administration (generally recognized as safe, GRAS; Notice, no. 773). To attach NP(DOX) to the algae surface, we used a straightforward click chemistry approach, involving bridging dibenzocyclooctyne (DBCO)-modified microalgae with azido-functionalized NP(DOX) (Fig. 1G and fig. S2). The binding of NP(DOX) was visually confirmed using fluorescence imaging (fig. S3). Enlarged images showed individual algae, with their chloroplast autofluorescence, surrounded by punctate signal originating from NP(DOX) (Fig. 1H). Binding of NP(DOX) to microalgae was further confirmed by SEM, which also revealed negligible damage caused by the binding process with the microalgae retaining their two flagella (Fig. 1I). The optical absorption spectrum of algae-NP(DOX)-robots exhibited absorption peaks at wavelengths of 480 and 680 nm, corresponding to the absorption of DOX and algae chlorophyll a, respectively (Fig. 1J) (52). The loading of DOX onto the microalgae could be controlled by varying the initial input DOX concentration (Fig. 1K). A DOX loading capacity as high as $27 \mu\text{g}$ per 1×10^6 microalgae was obtained upon increasing the drug input concentration. In particular, a saturation level was achieved at approximately $50 \mu\text{g}$ of drug input, corresponding to a binding efficiency of 46%. The binding efficiency dropped markedly upon increasing the drug input concentration, ranging from 73 wt % at the lowest measured input of $6.25 \mu\text{g}$ down to 27.4 wt % at the highest input of $100 \mu\text{g}$ (fig. S4). Flow cytometry studies were conducted to quantify the percentage of the algae population that could be bound with NP(DOX). It was found that when 1×10^6 algae were mixed with $25 \mu\text{g}$ of DOX in NP(DOX), 83.9% of them were positive for nanoparticle signal; this percentage rose to 96.3% upon raising the NP(DOX) input to $100 \mu\text{g}$ (Fig. 1L and fig. S5).

Motion behavior and in vitro characterizations of algae-NP(DOX)-robot

Microalgae exhibit various autonomous functions, such as self-propulsion and phototaxis, allowing them to respond to the environment (38). These characteristics can be harnessed for designated tasks to support the operation of biohybrid microrobots. We therefore investigated the impact of drug loading on the functional properties of microalgae. The speed and percentage of motile biohybrid microrobots with different drug inputs were first measured in water at 22°C (Fig. 2, A and B, and movie S1). Algae-NP(DOX)-robot maintained a steady speed of $\sim 100 \mu\text{m s}^{-1}$ and a high motility ratio at DOX inputs of 6.25 and $25 \mu\text{g}$, respectively. However, when the DOX input was increased to $100 \mu\text{g}$, only 52% of algae robots remained motile, with the average speed being reduced to $82.9 \mu\text{m s}^{-1}$. Such decline is attributed to the higher nanoparticle payload, potentially affecting the flagella beating and microalgae motility. Consequently, a DOX input of $25 \mu\text{g}$ was selected for subsequent in vitro and in vivo studies. Representative characteristic fluorescence motion tracking trajectories of a single algae-NP(DOX)-robot over a 2-s period are

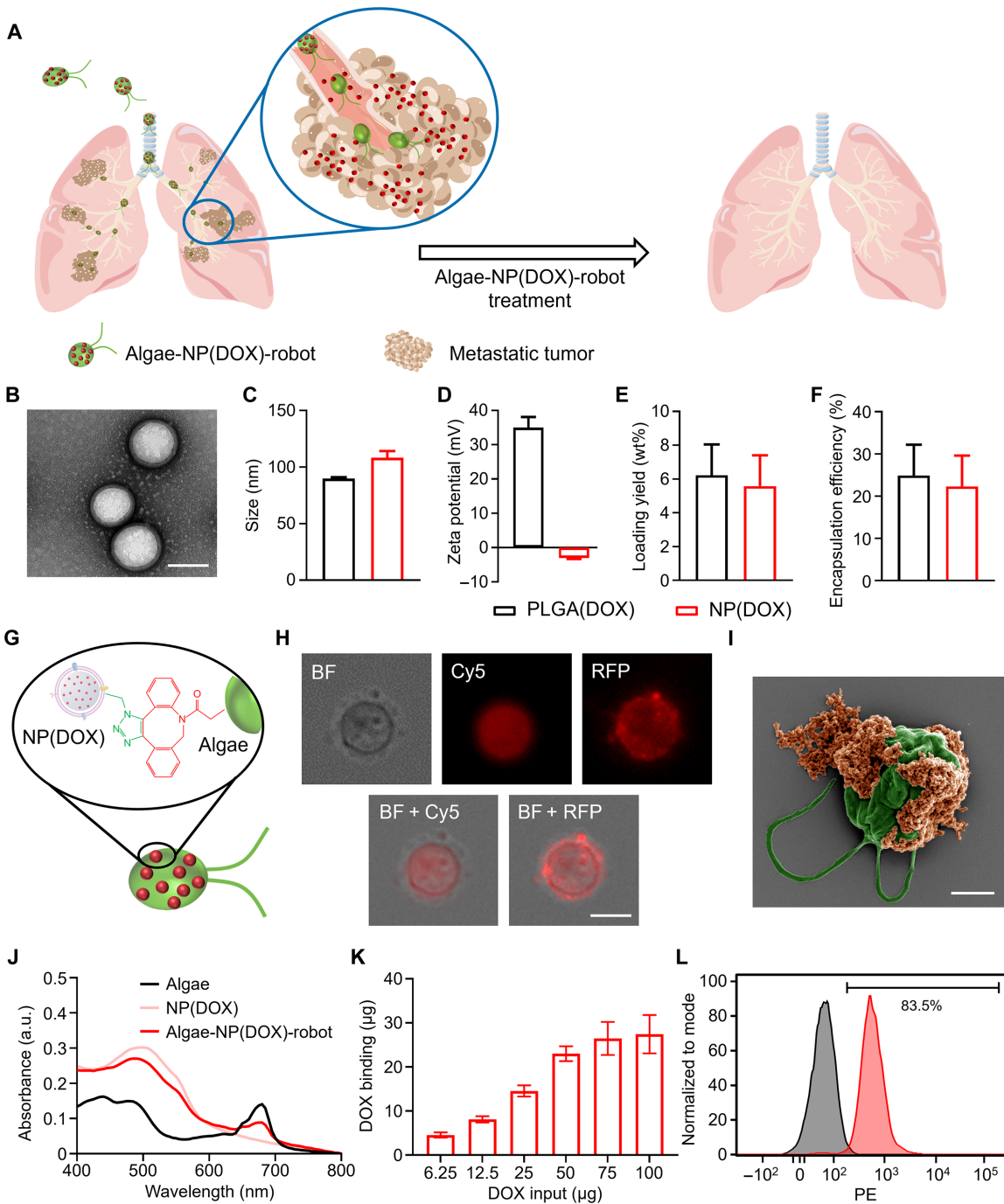


Fig. 1. Preparation and characterization of algae-NP(DOX)-robot. (A) Schematic depicting the use of algae-NP(DOX)-robot for the treatment of melanoma lung metastasis. (B) Transmission electron microscopy image of RBC membrane-coated DOX-loaded nanoparticles [denoted NP(DOX)]. Scale bar, 100 nm. (C and D) Size (C) and surface zeta potential (D) of NP(DOX) and bare DOX-loaded polymeric nanoparticles [denoted PLGA(DOX)] ($n = 3$; mean \pm SD). (E and F) Drug loading yield (E) and encapsulation efficiency (F) of NP(DOX) and PLGA(DOX) ($n = 3$; mean \pm SD). (G) Schematic illustration of algae-NP(DOX)-robot, in which NP(DOX) is covalently conjugated onto algae via click chemistry. (H) Representative bright-field (BF) and fluorescent images of an algae-NP(DOX)-robot. Autofluorescence of algae chloroplast in the Cy5 channel; NP(DOX) in the RFP channel. Scale bar, 10 μ m. (I) Pseudo-colored SEM image of an algae-NP(DOX)-robot. Algae in green; NP(DOX) in orange. Scale bar, 2 μ m. (J) Optical absorption spectrum of algae-NP(DOX)-robot compared with bare algae and NP(DOX). a.u., arbitrary units. (K) Quantification of DOX loading on 1×10^6 algae at various initial drug inputs ($n = 3$; mean \pm SD). (L) Representative flow cytometry histograms of algae before (gray) and after (red) functionalization with NP(DOX) at a 25- μ g drug input. DOX is measured on the phycoerythrin (PE) channel.

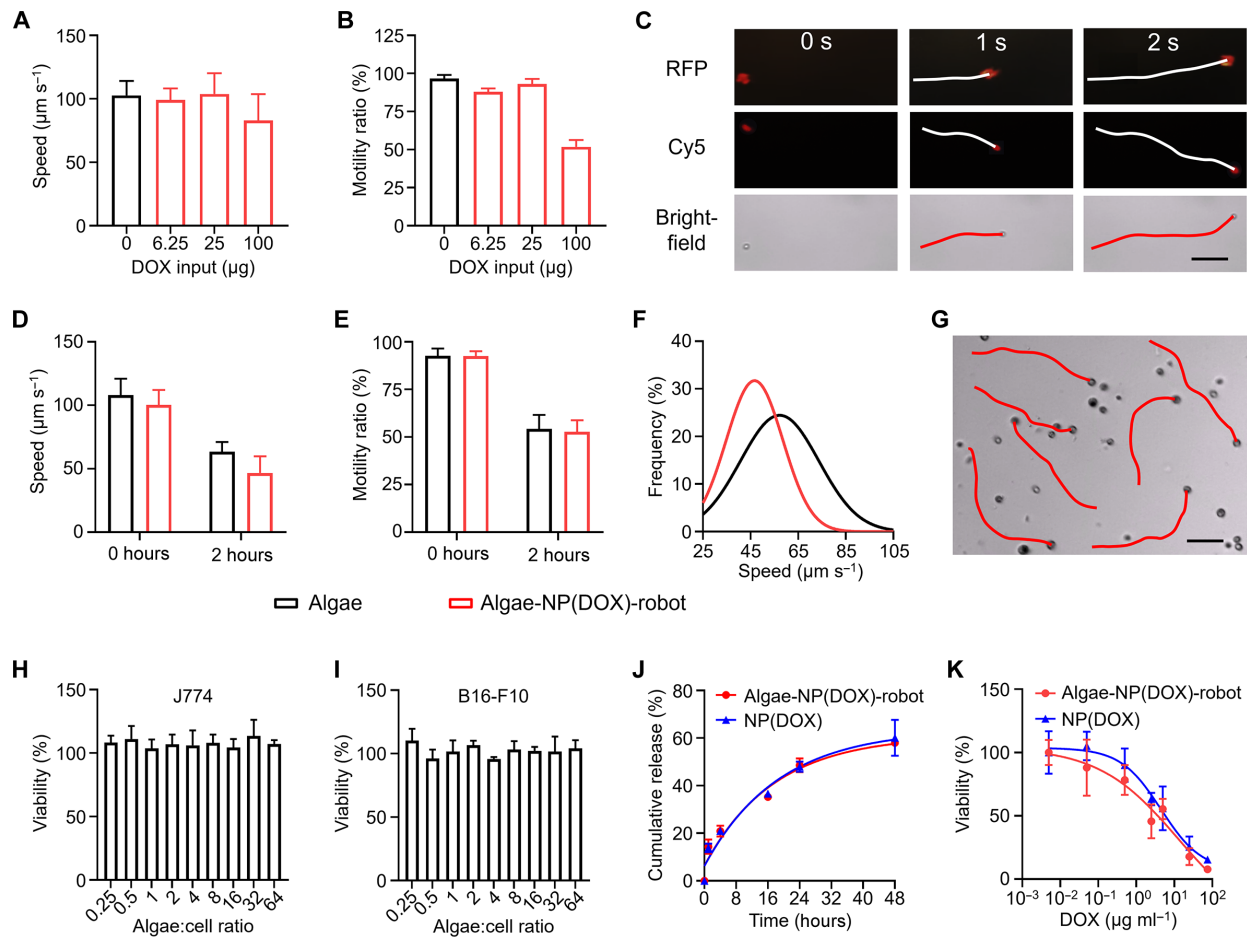


Fig. 2. Motion behavior and in vitro characterizations of algae-NP(DOX)-robot. (A and B) Speed (A) and motility ratio (B) of algae-NP(DOX)-robot at different drug inputs in water at 22°C [$n = 10$ for (A) and $n = 5$ for (B); mean \pm SD]. (C) Snapshot of self-propelled motion of algae-NP(DOX)-robot over 2 s in water at 22°C under fluorescence and optical microscopes. NP(DOX) in the RFP channel; autofluorescence of alga chloroplast in the Cy5 channel. Scale bar, 50 μm . (D) Speed (D) and motility ratio (E) of bare algae and algae-NP(DOX)-robot before and after 2 hours of motion in SLF at 37°C [$n = 10$ for (D) and $n = 5$ for (E); mean \pm SD]. (F) Swimming velocity analyses of bare algae and algae-NP(DOX)-robot after 2 hours of motion in SLF at 37°C. (G) Swimming trajectories of algae-NP(DOX)-robot over 5 s in SLF at 37°C. Scale bar, 50 μm . (H and I) Viability of J774 macrophages (H) and B16-F10 cancer cells (I) after 24 hours of incubation with NP-functionalized algae without DOX at varying algae-to-cell ratios ($n = 3$; mean \pm SD). (J) Drug release profiles of algae-NP(DOX)-robot and NP(DOX) ($n = 3$; mean \pm SD). (K) In vitro anticancer activity of NP(DOX) and algae-NP(DOX)-robot against B16-F10 melanoma cells after 24 hours of incubation ($n = 3$; mean \pm SD).

displayed in Fig. 2C and movie S2. These illustrate that the moving microrobots could be tracked continuously via fluorescence imaging without further modifications. To mimic conditions in pulmonary delivery, the motion features of the microrobots were examined also in simulated lung fluid (SLF) at 37°C (Fig. 2, D and E, and movie S3). After 2 hours of incubation, the speed of the algae-NP(DOX)-robots decreased from 100.3 to 46.7 $\mu\text{m s}^{-1}$, showing a similar trend to the algae without NP(DOX) conjugation. The corresponding motility ratio of microrobots decreased from 92.5 to 52.8% after 2 hours, which was also comparable to the change for the bare algae group. The alterations in speed and reduced motility are attributed to the effect of the higher temperature on the synthesis and function of the dynein protein, which, in turn, affects the beating of flagella (53). To further evaluate the impact of the NP(DOX) conjugation on the algae motility, the mean speed distribution of the algae-NP(DOX)-robots after 2 hours of operation at 37°C was also analyzed (Fig. 2F). We observed the speed of 100 algae for both algae-NP(DOX)-robots and bare algae and found that the speed of algae-NP(DOX)-robots

decreased slightly, with 80% of them moving within the range of 35 to 75 $\mu\text{m s}^{-1}$, whereas 80% of bare algae retained speeds in the range of 40 to 80 $\mu\text{m s}^{-1}$. The movement patterns of biohybrid microrobots in the SLF at 37°C was also evaluated. Algae-NP(DOX)-robot exhibited a smooth and random motion, similar to the typical movement path of bare algae shown in movie S1, suggesting that the binding of NP(DOX) onto the alga body did not affect the flagella beating (Fig. 2G). It should be noted that 98% of algae-NP(DOX)-robots retained their viability even after a 16-hour incubation in SLF, demonstrating their impressive adaptability and ability to operate under conditions mimicking the lung environment (fig. S6). Furthermore, the NP(DOX) displayed robust binding to the alga surface after a 48-hour incubation in SLF at 37°C, with 97% of NP(DOX) bound to microalgae, providing additional evidence for the stability of the microrobot system (fig. S7).

For biomedical applications, it is imperative that microrobots exhibit minimal cytotoxicity. To test the cytotoxicity of the biohybrid microrobots, we incubated NP-functionalized algae that were not loaded

with DOX with both immune cells (J774 macrophage cells) and cancer cells (B16-F10 melanoma cells). Using an 3-(4,5-dimethylthiazol-2-yl)-5-(3-carboxymethoxyphenyl)-2-(4-sulfophenyl)-2H-tetrazolium (MTS) assay to measure the viability of cells treated with varying algae-to-cell ratios, no significant differences compared with the untreated control group were observed (Fig. 2, H and I). We then evaluated the drug release profiles of both NP(DOX) and algae-NP(DOX)-robot in SLF at 37°C (Fig. 2J). It was shown that the cumulative drug release characteristics of NP(DOX) remained unaffected when bound to the algae microrobots. To assess the in vitro anticancer efficiency of algae-NP(DOX)-robots, we subsequently explored their effects on B16-F10 melanoma cells in comparison with NP(DOX) (Fig. 2K). The dose-responsive curves indicate that the microrobot group was more effective in killing the cancer cells when compared to the NP(DOX) group. It is noteworthy to emphasize that the anticancer effects are attributed solely to the functionality of DOX, as the NP-functionalized algae (without DOX) had no impact on the proliferation of B16-F10 cells as shown in Fig. 2I. Furthermore, at a concentration of 1 mg/ml DOX, significantly above the levels used in our in vitro and following in vivo experiments, the drug did not cause noticeable toxicity to the microalgae after 24 hours of incubation in water at 37°C, while at 2 mg/ml, viability decreased to 75% and further declined to 40% at 4 mg/ml (fig. S8). These findings suggest that the algae-NP(DOX)-robot exhibits potent effectiveness in inhibiting the growth and proliferation of cancer cells, thus holding promise as a platform for cancer treatment.

In vivo biodistribution and drug retention of algae-NP(DOX)-robot

We next evaluated whether the biohybrid microrobots could be used to deliver anticancer drugs to the lungs and improve the drug retention. A DOX dose of 75 µg per mouse was intratracheally administered to test the delivery efficiency. Following intratracheal administration, the lungs were collected to examine the distribution of both the drug and the microalgae carriers at various time points. Microalgae and DOX exhibit distinct non-overlapping fluorescence emission peaks at 680 and 590 nm, respectively (fig. S9). This feature enables their selective detection using fluorescence imaging without interference. Ex vivo fluorescence imaging revealed that DOX was detectable in both the algae-NP(DOX)-robot and NP(DOX) groups (Fig. 3A), whereas only the algae-NP(DOX)-robot group exhibited a robust signal corresponding to chloroplast autofluorescence (Fig. 3B and fig. S10). To accurately quantify drug retention in the lungs, we used a highly sensitive liquid chromatography–mass spectrometry (LC-MS) technique. At 0 hours, both groups contained approximately 70 µg of DOX, which was comparable to the 75-µg dose that was administered, suggesting that most of the drug was successfully delivered to the lung (Fig. 3C). At later time points (4 and 24 hours), the remaining drug in the algae-NP(DOX)-robot group was 2.5- and 4.4-fold higher, respectively, compared to the NP(DOX) group (Fig. 3, D and E). When normalized to the input, 62.7 and 9.4% of the drug in the algae-NP(DOX)-robot group was retained at 4 and 24 hours, respectively; in contrast, only 25.5 and 2.1% of the drug remained after NP(DOX) administration at the same time points (fig. S11). Furthermore, we evaluated the histological distribution of the algae-NP(DOX)-robot within the lungs at 24 hours after administration (Fig. 3F). Stronger DOX fluorescence was observed in lung sections treated with algae-NP(DOX)-robot compared to those treated

with NP(DOX), consistent with the quantitative retention data. The algae autofluorescence colocalized well with DOX in the bronchioles, indicating the stability of the chemically bonded NP(DOX) after delivery. In addition, the algae-NP(DOX)-robot delivered DOX deep into the tissue, whereas little DOX was found in the same regions for the NP(DOX) group. Quantification of the fluorescence in the lung sections revealed a 5.5-fold higher level of DOX for mice receiving algae-NP(DOX)-robots (Fig. 3G).

To better understand the enhanced drug distribution and retention of the algae-NP(DOX)-robots compared to NP(DOX), we investigated a potential clearance mechanism from the lungs. Alveolar macrophages, which are lung-resident immune cells that express specific surface markers such as Siglec-F and CD11c, play a crucial role in surfactant clearance and immune surveillance. Our previous work has demonstrated that motile microalgae exhibited a greatly reduced uptake by macrophages both in vitro and in vivo compared to static algae control (29). To explore how they might function in vivo in the lungs, we investigated here the interaction between macrophages and two types of drug carriers, algae-NP(DOX)-robots and NP(DOX), in vitro. Specifically, murine J774 macrophages were exposed to these carriers separately at 37°C to assess DOX uptake over different time periods. Following a 24-hour incubation, it was observed that only 23.0% of DOX carried by microrobots was engulfed, whereas 70.7% of DOX in the nanoparticle group were taken up (fig. S12). This finding supports the notion that the use of microrobots hinders nanoparticle uptake compared to conventional nanoparticle delivery methods. In vivo, flow cytometry analysis was conducted to assess the interaction between alveolar macrophages and algae-NP(DOX)-robots at various time points following intratracheal administration (Fig. 3, H and I). When looking at the CD11c⁺Siglec-F⁺ population in the bronchoalveolar lavage fluid (BALF), minimal DOX uptake was observed over the initial 4 hours in the case of algae-NP(DOX)-robot, with increased uptake occurring after at 8 hours; in contrast, alveolar macrophages in the NP(DOX) group exhibited elevated uptake after only 1 hour (Fig. 3H). The delayed uptake of DOX in algae-NP(DOX)-robot was consistent with the uptake profile of the algal component over the same time period (Fig. 3I) and thought to be attributed to the motility of microalgae, which allows them to evade macrophage uptake. Once ingested by the alveolar macrophage, the microalgae undergo degradation into smaller components, such as amino acids and sugars, through enzymatic action within the macrophage lysosome. Ultimately, this process leads to the complete clearance of the microrobots. Such clearance mechanism was supported by the decreased microalgae fluorescence observed during the phagocytosis process (fig. S13). In essence, the self-propulsion of microalgae generates actuation power within the lungs of mice, enabling the biohybrid robots to evade uptake by alveolar macrophages, consistent with previous findings (29). Such behavior appears to reflect the enhanced accumulation and prolonged retention of the drug payload NP(DOX) within the lungs.

In vivo anticancer therapeutic efficacy of algae-NP(DOX)-robot

We further established a B16-F10-Luc2 melanoma lung metastasis model to evaluate the antimetastatic efficacy of the algae-NP(DOX)-robot platform (Fig. 4A). This model was established by intravenously injecting 1×10^5 B16-F10-Luc2 cells through the tail vein of C57BL/6 mice. The treatment regimen consisted of four 75-µg DOX

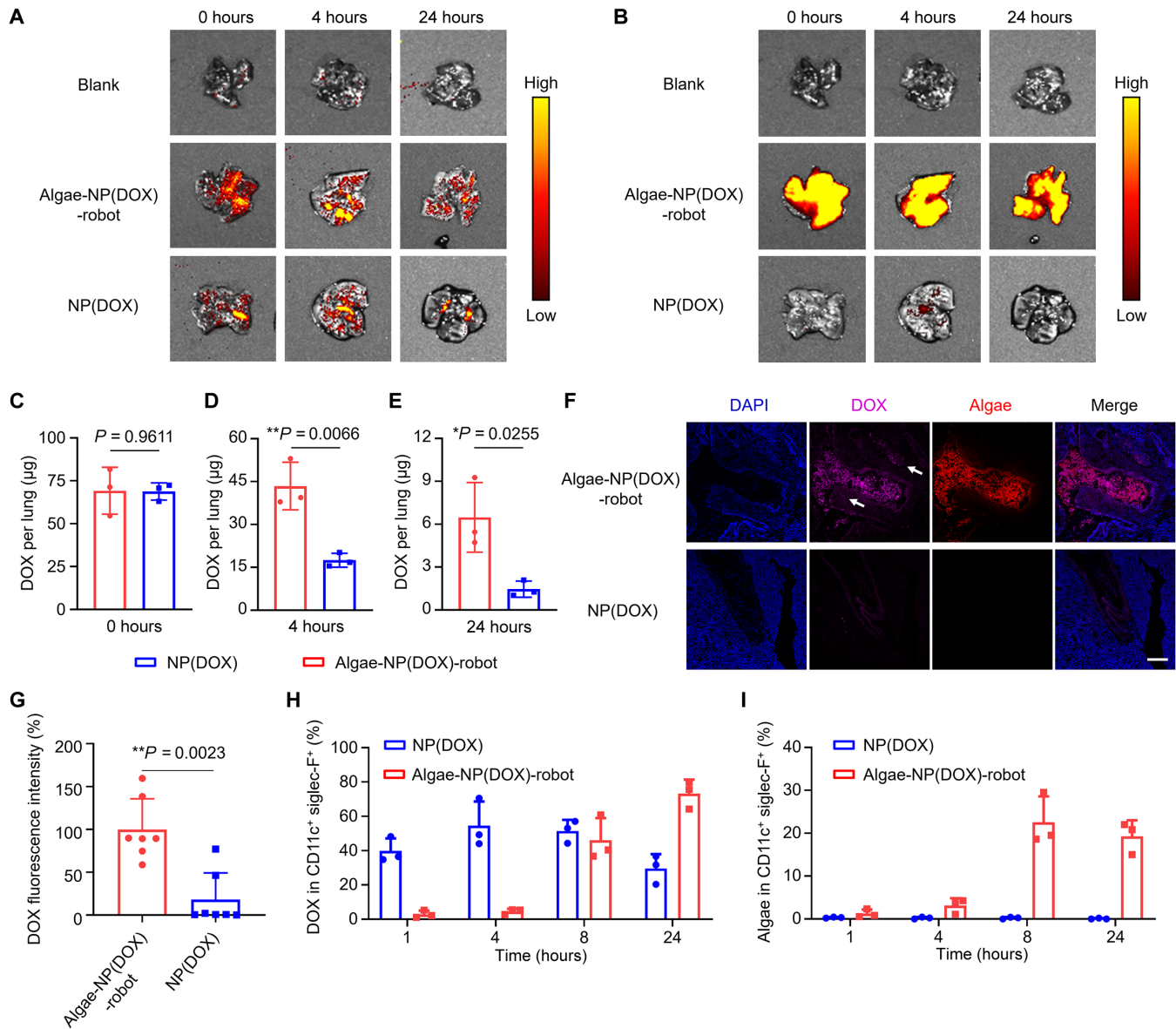


Fig. 3. In vivo biodistribution and drug retention of algae-NP(DOX)-robot. (A and B) Lung distribution of DOX (A) and microalgae (B) examined by ex vivo fluorescence imaging at various time points after intratracheal administration of algae-NP(DOX)-robot or NP(DOX). (C to E) Drug accumulation in the lungs at 0 hours (C), 4 hours (D), and 24 hours (E) after intratracheal administration of algae-NP(DOX)-robot or NP(DOX) ($n = 3$; mean \pm SD). (F) Representative lung tissue section showing DOX distribution at 24 hours after intratracheal administration of algae-NP(DOX)-robot or NP(DOX). White arrows indicate the signal from DOX penetrated the deep lung tissue. Scale bar, 200 μ m. DAPI, 4',6-diamidino-2-phenylindole. (G) Lung drug retention based on the quantification of total DOX fluorescence intensity in histological sections ($n = 7$; mean \pm SD). (H and I) DOX (H) and algae (I) uptake in alveolar macrophage at various time points after intratracheal administration of algae-NP(DOX)-robot or NP(DOX) ($n = 3$; mean \pm SD). Student's *t* test for (C) to (E) and (G), * $P < 0.05$ and ** $P < 0.01$.

doses given every other day, with the first dose administered 1 day after the tumor challenge. The progression of lung metastasis was evaluated by measuring bioluminescence intensity in the lungs, and significantly better inhibition of lung metastasis progression was observed for the algae-NP(DOX)-robot group as compared to the free drug or NP(DOX) control groups (Fig. 4, B and C). The signals observed in other organs could be due to inadequate treatment causing tumor cell migration to additional tissues. We also quantified the overall lung metastasis burden based on the bioluminescence intensity

in the lungs (Fig. 4D). During the first 20 days after tumor inoculation, lung metastasis was nearly completely suppressed in mice treated with algae-NP(DOX)-robot. In particular, the total bioluminescence intensity for the algae-NP(DOX)-robot group was 88.7-fold lower compared with the blank control. On day 24, treatment using algae-NP(DOX)-robots led to a 19.6- and 38.2-fold lower total bioluminescence intensity compared to free DOX and NP(DOX), respectively (Fig. 4E). Survival analysis further validated the significantly improved therapeutic benefit of the algae-NP(DOX)-robots (Fig. 4F).

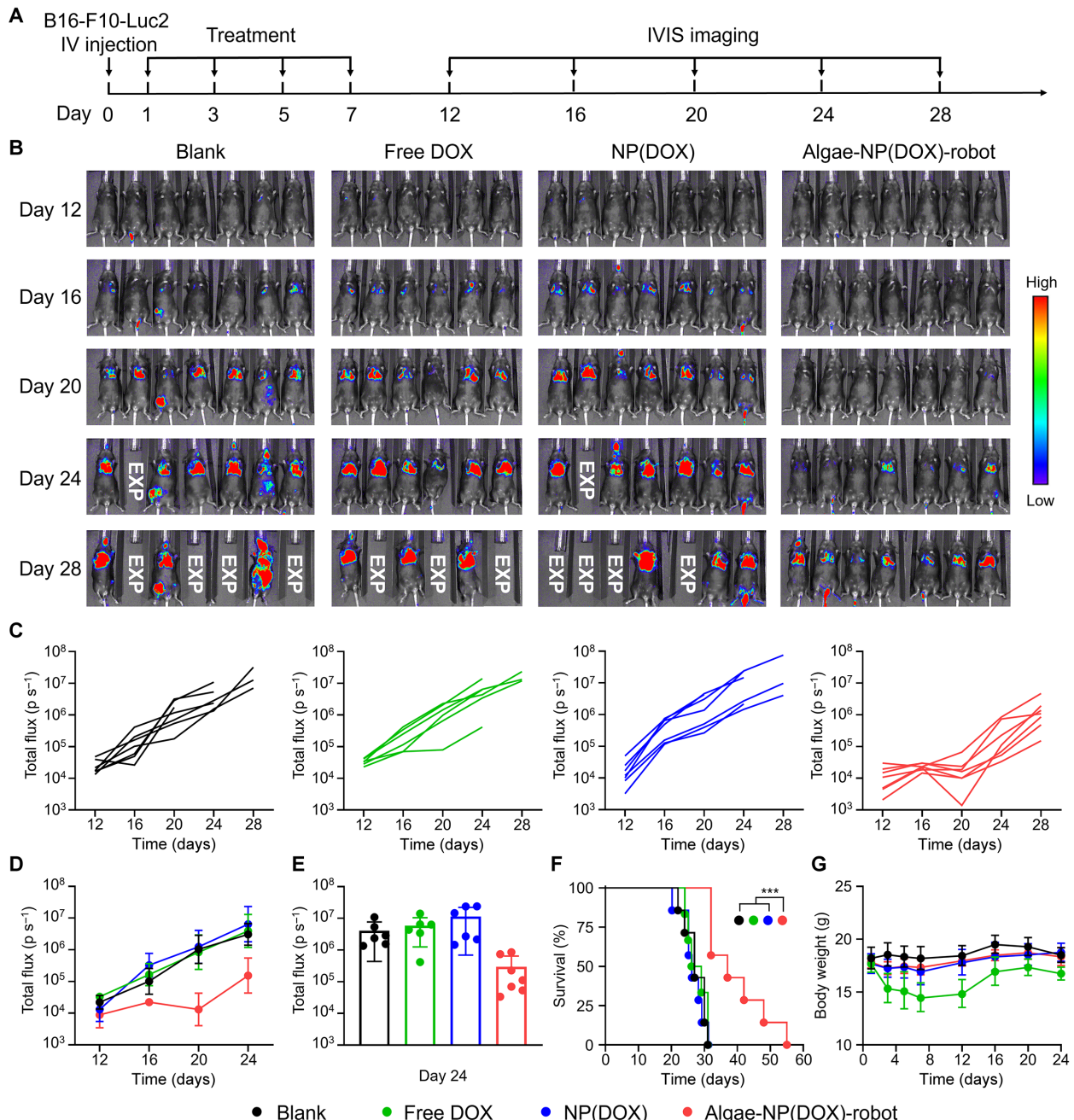


Fig. 4. Therapeutic efficacy of algae-NP(DOX)-robot against melanoma lung metastasis. (A) Schematic diagram showing the experimental timeline; mice were treated with free DOX, NP(DOX), or alga-NP(DOX)-robot. IV, intravenous. (B) Bioluminescence images of mice at different time points. (C) Quantification of bioluminescence intensity of individual mice over time ($n = 6$ or 7). (D) Quantification of total bioluminescence intensity over time ($n = 6$ or 7; mean \pm SD). (E) Comparison of total bioluminescence intensity on day 24 ($n = 6$ or 7; mean \pm SD). (F) Survival after treatment ($n = 6$ or 7). (G) Body weight over time ($n = 6$ or 7; mean \pm SD). Log-rank (Mantel-Cox) test for (F), *** $P < 0.001$ [compared to alga-NP(DOX)-robot].

Whereas free drug and NP(DOX) control treatments did not enhance survival, with a median survival time of 27 days, the group treated with alga-NP(DOX)-robots experienced a 40% increase in median survival time, extending it to 37 days. In addition, we monitored for changes in body weight during the entire treatment period (Fig. 4G). No significant body weight loss was observed in the alga-NP(DOX) and NP(DOX) treatment groups. However, a pronounced

decline in body weight was evident during the first 7 days of free DOX treatment, indicating the presence of some toxicity.

In vivo toxicity assessment of alga-NP(DOX)-robot in healthy mice

Last, the toxicity profile of the alga-NP(DOX)-robot was assessed. Healthy mice were subjected to intratracheal administration using

one of three different treatments: algae-NP(DOX)-robot, free DOX, and NP(DOX). Each mouse received a total of four 75- μg DOX doses given every other day. A blood count and a comprehensive metabolic panel were performed 1 day after the final injection to assess the effects of these treatments. We examined the levels of several biomarkers commonly associated with liver and kidney functions, including albumin, alkaline phosphatase, alanine transaminase, blood urea nitrogen, total bilirubin, and creatinine, and found no abnormalities (Fig. 5A). Other biomarkers such as calcium, glucose, phosphorus, potassium, sodium, and total protein

were also found to be within their normal ranges. Furthermore, we confirmed the absence of any significant hematologic abnormalities resulting from algae-NP(DOX)-robot treatment, as the levels of white blood cells, RBCs, and platelets all remained within the normal limits (Fig. 5B). Notably, the free drug group displayed elevated platelet levels, again indicating a certain degree of toxicity. Histological examination of tissue sections, including the heart, liver, spleen, lungs, and kidneys, revealed no observable damage (Fig. 5C). Collectively, these data indicate the favorable safety characteristics of the algae-NP(DOX)-robot delivery platform in healthy mice.

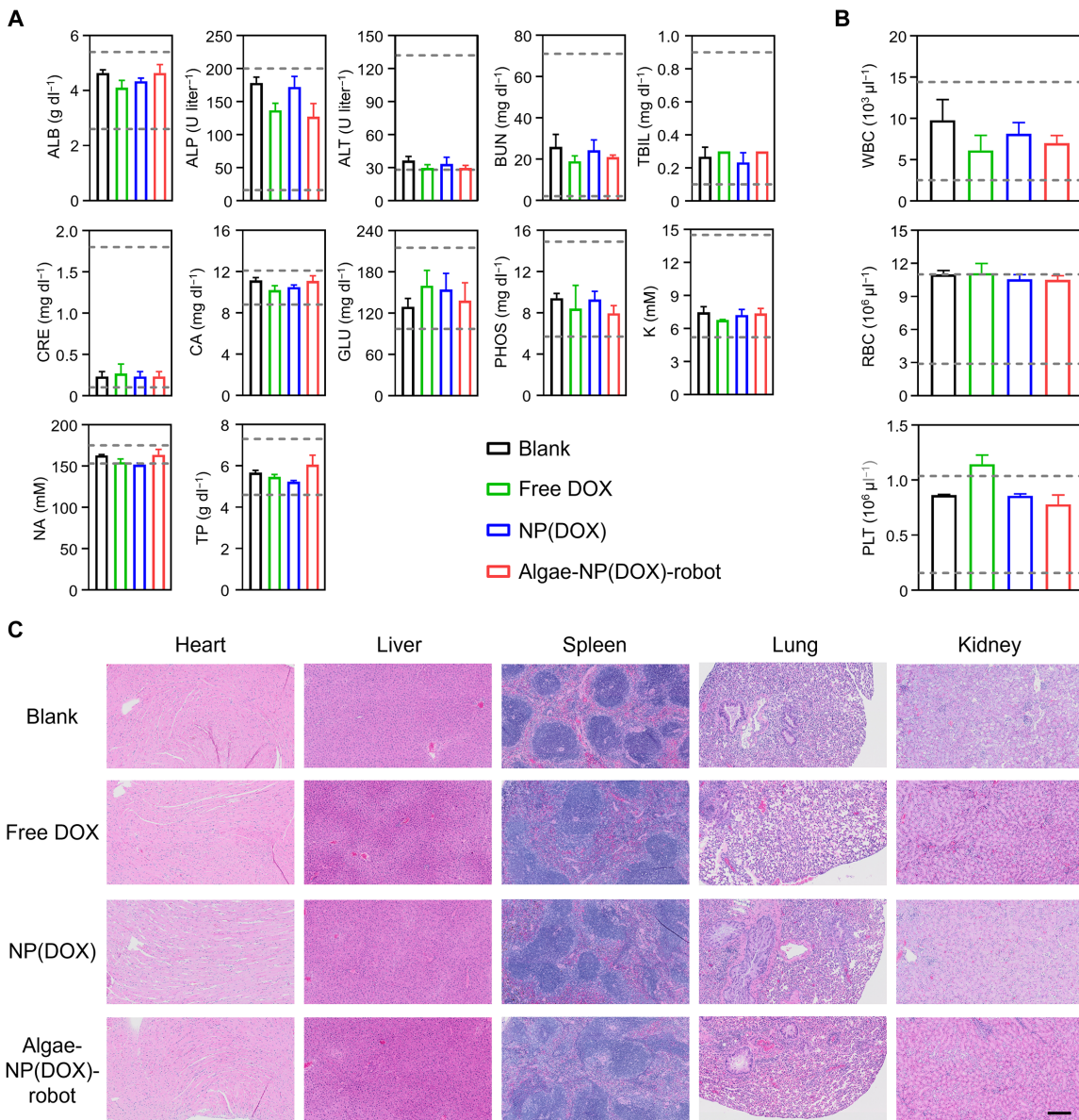


Fig. 5. In vivo safety evaluation of algae-NP(DOX)-robot. (A and B) Comprehensive blood chemistry panel (A) and blood cell counts (B) of untreated mice, as well as mice administered intratracheally with free DOX, NP(DOX), or algae-NP(DOX)-robot on days 0, 2, 4, and 6 ($n = 3$; mean \pm SD); blood samples were collected 24 hours after the last dose. ALB, albumin; ALP, alkaline phosphatase; ALT, alanine transaminase; BUN, blood urea nitrogen; TBIL, total bilirubin; CRE, creatinine; CA, calcium; GLU, glucose; PHOS, phosphorus; K, potassium; NA, sodium; TP, total protein; WBC, white blood cell; RBC, red blood cell; PLT, platelet. The gray dashed lines represent the mouse reference ranges for each parameter. (C) Hematoxylin and eosin-stained histological sections of major organs, including the heart, liver, spleen, lungs, and kidneys, from untreated mice and mice administered intratracheally with free DOX, NP(DOX), or algae-NP(DOX)-robot on days 0, 2, 4, and 6; tissue samples were collected 24 hours after the last dose. Scale bar, 200 μm .

DISCUSSION

In summary, we have demonstrated an attractive approach to engineering living microalgae as a biohybrid microrobotic vehicle to deliver nanotherapeutics into deep lung tissues for the treatment of lung metastasis. Synthetic cell membrane-coated anticancer drug-loaded nanoparticles were bound to the microalgae surface via click chemistry. The linking of the nanoparticles had no effect on either the intrinsic motility of the microalgae or the anticancer activity of the drug payload. Through intratracheal administration, the drug transported by the biohybrid microrobots can be localized within the lungs, minimizing side effects to other organs. The traditional pharmacokinetic assessments in blood and biodistribution in other organs do not apply to this study due to the localized delivery method. Compared with free drug and drug-loaded nanoparticles, the biohybrid microrobots exhibited enhanced tissue accumulation and extended retention in the deep lungs. The prolonged drug retention could be attributed to the unique motion capability of the microalgae, which enables them to evade phagocytosis by alveolar macrophages. Using a mouse model of lung metastasis, we demonstrated the effectiveness of our biohybrid microrobot formulation in delivering DOX to diseased lung tissues, which significantly improved therapeutic outcomes by reducing lung metastasis burden and extending median survival time. While our data suggest that robotic motion contributes to enhanced drug retention and antitumor efficacy, it will be necessary to delve into additional factors, such as bioadhesion, size effects, and clearance rate to better understand the precise mechanics of robotic deep lung penetration in future studies. Overall, the combination of motile living microalgae and cell membrane-coated drug-loaded nanoparticles presents a powerful approach to pulmonary drug delivery and lays the foundation for engineered biohybrid microrobots in lung metastasis therapy. Looking ahead from a robotic perspective, we acknowledge the high potential of integrating additional motion control strategies, such as magnetic guidance or ultrasound trapping (24, 54, 55), in disease models that require enhanced accumulation at specific targeted sites.

MATERIALS AND METHODS

Green algae culture

C. reinhardtii (CC-125 wild-type mt+) was sourced from the Chlamydomonas Resource Center. The strain was cultivated in tris-acetate-phosphate medium (Thermo Fisher Scientific) at room temperature (approximately 22°C) with alternating cycles of 12 hours of exposure to sunlight and 12 hours of darkness.

Preparation of PLGA(DOX) and NP(DOX)

DOX-loaded PLGA nanoparticles [PLGA(DOX)] were prepared following a previously reported method (49). First, the nanoparticle cores were synthesized by a nanoprecipitation technique. Briefly, 20 mg of PLGA (50:50, 0.67 dL/g, Lactel Absorbable Polymers) was dissolved in 1 ml of acetone. Subsequently, 5 mg of DOX (Sigma-Aldrich) was dissolved in 500 μl of methanol containing 5 μl of triethylamine. After thoroughly mixing the DOX solution with the PLGA solution, the combined mixture was added dropwise into 10 ml of 1% polyvinyl alcohol solution under 700 rpm stirring. The organic solvent was then evaporated through overnight stirring. To determine the amount of drug loaded into the PLGA nanoparticles, 1 ml of PLGA(DOX) solution was centrifuged for 5 min at 16,100g, and the supernatant was discarded. The pellet was subsequently

dissolved in dimethyl sulfoxide (Sigma-Aldrich) and vortexed at 700 rpm for 15 min to fully release the DOX from the PLGA core. The concentration of DOX was measured using a Tecan Infinite M200 plate reader (excitation/emission = 480/590 nm).

NP(DOX) were synthesized using a previously established membrane coating technique (50). Specifically, RBCs were collected from 6-week-old male ICR (CD-1) mice (Charles River Laboratories) by centrifuging whole blood at 800g for 5 min, followed by hypotonic treatment to remove interior contents. The obtained RBC ghost was combined with PLGA(DOX) cores at a 1:2 membrane protein-to-polymer weight ratio. The resulting mixture was then subjected to sonication for 3 min using a Fisherbrand 11201 series bath sonicator. Subsequently, the NP(DOX) were isolated by centrifugation for 5 min at 16,100g and washed three times with ultrapure water.

The hydrodynamic size and zeta potential of the PLGA(DOX) and NP(DOX) were assessed both before and after the cell membrane coating by dynamic light scattering using a Malvern ZEN 3600 Zetasizer. An FEI Sphera transmission electron microscope operating at 200 kV was used for visualizing the morphology of the NP(DOX) stained with 0.2 wt % uranyl acetate. For SEM characterization, NP(DOX) were sputtered with palladium for imaging on a Zeiss Sigma 500 scanning electron microscope at an acceleration voltage of 3 kV.

Preparation of algae-NP(DOX)-robot

Cultured algae were washed five times using ultrapure water by centrifuging at 500g for 3 min. The concentration of the algae was then adjusted to 1×10^7 cells ml⁻¹. Next, 1 ml of algae solution was incubated with 4 μl of 10 mM azido-PEG₄-N-hydroxysuccinimide (NHS) ester (Click Chemistry Tools) for 1 hour at room temperature (22°C). Concurrently, 1 ml of 1 mg ml⁻¹ NP(DOX) in ultrapure water was combined with 4 μl of 10 mM DBCO-PEG₄-NHS ester (Click Chemistry Tools) for 1 hour at room temperature (22°C). After the incubations, both the azido-labeled algae and DBCO-labeled NP(DOX) were washed four times with ultrapure water by centrifuging at 500g for 2 min for the algae and at 16,100g for 3 min for NP(DOX). The conjugation was executed by mixing 1×10^6 azido-labeled algae with varying amounts of DBCO-labeled NP(DOX) (6.25, 12.5, 25, 50, 75, and 100 μg) for 1 hour at room temperature (22°C). Following conjugation, the samples were washed three times with ultrapure water to remove free NP(DOX) by centrifuging at 500g for 2 min. Last, the resulting algae-NP(DOX)-robots were stored in ultrapure water for further use.

Characterization of algae-NP(DOX)-robot

To prepare algae-NP(DOX)-robot for SEM imaging, fixation was performed by combining it with a 5% glutaraldehyde solution (Sigma-Aldrich) in a 1:1 volume ratio. The fixed samples were then stored overnight at 4°C. Afterward, the samples were washed three times with ultrapure water by centrifuging at 100g for 2 min, after which they were left to dry overnight. Subsequently, the samples were coated with iridium and imaged using a Zeiss Sigma 500 scanning electron microscope at an acceleration voltage of 3 kV. Fluorescent microscopy (Evos FL) was used to examine the autofluorescence of the algae and DOX loaded in the PLGA cores under the Cyanine-5 (Cy5) and red fluorescent protein (RFP) channels, respectively. The fluorescence spectrum of both microalgae and DOX in water was measured using a BioTek Synergy Mx microplate reader, with an excitation wavelength at 440 nm. To determine

the percentage of algae bound with NP(DOX), various quantities of NP(DOX) were coincubated with the algae and then washed three times by centrifuging at 500g for 2 min to remove unbound NP(DOX). These algae-NP(DOX)-robot samples were then resuspended in deionized water for flow cytometry analysis. The data were collected using a Becton Dickinson LSR II flow cytometer and analyzed with FlowJo v10.4 software. To test the stability of NP(DOX) bound to microalgae, we initially conjugated NHS-fluorescein isothiocyanate (FITC) to the surface of RBC membrane on the NP(DOX). The as-prepared FITC-labeled NP(DOX) were chemically bound to microalgae for the fabrication of algae-NP(DOX)-robot using the identical click chemistry method described above. These micro-robots were then incubated in SLF at 37°C. The fluorescence-bound FITC-labeled NP(DOX) was measured at various time points (0, 1, 2, 8, 12, 24, and 48 hours) using a microplate reader at $\lambda_{\text{ex}}/\lambda_{\text{em}} = 484/501$ nm. The percentage of bound NP(DOX) was determined by converting the measured fluorescence intensity using a FITC standard curve.

Motion analysis

Bare algae and algae-NP(DOX)-robots with various NP(DOX) inputs (6.25, 25, and 100 µg) were suspended in SLF at room temperature (22°C) to measure their speed and motility ratio. The SLF was prepared on the basis of the previous reference (29). Algae-NP(DOX)-robot with a 25-µg NP(DOX) input were subjected to further analysis at body temperature (37°C) in SLF at 0 and 2 hours. Furthermore, to visualize the trajectory of algae-NP(DOX)-robots, motion tracking lines were recorded over 2 s in the bright-field, Cy5, and RFP channels. All motion videos were taken by a Nikon Eclipse Ti-S/L100 inverted optical microscope equipped with a Hamamatsu C11440 digital camera under a Nikon 10× objective lens. The speed of the bare algae and algae-NP(DOX)-robot under various conditions was analyzed using the Nikon Instruments Software elements tracking module.

In vitro cytotoxicity of NP-functionalized algae without DOX

To assess the cytotoxicity of NP-functionalized algae without DOX, coincubation experiments were conducted in Dulbecco's modified Eagle's medium (DMEM; Thermo Fisher Scientific). J774 macrophage cells [American Type Culture Collection (ATCC) TIB-67] and B16-F10 (ATCC CRL-6475) cancer cells were seeded into 96-well plates at 1×10^5 per well. Varying concentrations of NP-functionalized algae without DOX were added to the cells, followed by incubation for 24 hours at 37°C. To test for any cytotoxicity, an MTS assay (Abcam) was subsequently incubated with the cells at 37°C for 45 min. Results were determined by measuring the absorbance at a wavelength of 490 nm using a BioTek Synergy Mx microplate reader.

In vitro DOX release from algae-NP(DOX)-robot

DOX release was evaluated by analyzing the supernatant from algae-NP(DOX)-robots and NP(DOX) at multiple time points, ranging from 0 to 48 hours. The concentration of DOX in the supernatant was quantified using a Tecan Infinite M200 plate reader (excitation/emission = 480/590 nm).

In vitro anticancer effects of algae-NP(DOX)-robot

To investigate the in vitro anticancer effects of algae-NP(DOX)-robots, B16-F10 cells were seeded into 96-well plates at a density of 1×10^6 per well in 100 µl of DMEM medium. After 24 hours, different

amounts of algae-NP(DOX)-robots or NP(DOX) containing 0.005, 0.05, 0.5, 2.5, 5, 25, and 75 µg ml⁻¹ of DOX were added to the wells. Cell viability was assessed after 24 hours using an MTS assay as described above.

Cytotoxicity of free DOX to microalgae

Toxicity of free DOX to microalgae was evaluated by incubating 1×10^4 microalgae with varying concentrations of free DOX (1, 2, and 4 mg/ml) for different durations (0, 2, 4, 12, and 24 hours). To assess algae viability, the dead algae were stained with 5 µM SYTOX green nucleic acid stain (Thermo Fisher Scientific).

In vitro macrophage uptake and clearance of algae-NP(DOX)-robot

J774A.1 macrophage cells were cultured in DMEM (Invitrogen) in a 24-well plate, with a density of 1×10^6 cells per well. Algae-NP(DOX)-robots were then added at a robot/macrophage ratio of 1:1 and incubated at 37°C. To test the DOX uptake by macrophages at specific time points of incubation (0, 2, 8, 12, 24, 48, and 72 hours), the unswallowed robots were removed, and the internalized DOX within macrophage was analyzed by fluorescence microscopy at $\lambda_{\text{ex}}/\lambda_{\text{em}} = 480/590$ nm. The fluorescence intensity was measured using a BioTek Synergy Mx microplate reader. The uptake of DOX in NP(DOX) group was evaluated and quantified by the same method. To test the microalgae clearance by macrophage, the mixture was analyzed by quantification of microalgae fluorescence intensity at $\lambda_{\text{ex}}/\lambda_{\text{em}} = 647/680$ nm over 72 hours.

Animal care

Six-week-old female C57BL/6 mice were purchased from Envigo and housed in an animal facility at the University of California San Diego (UCSD). All animal experiments were approved by the Institutional Animal Care and Use Committee of UCSD and performed under federal, state, local, and National Institutes of Health guidelines.

In vivo retention and lung distribution

Female C57BL/6 mice were anesthetized with a ketamine (Dechra) and xylazine (VetOne) cocktail and were then intratracheally administered with either algae-NP(DOX)-robot or NP(DOX), both containing a DOX dose of 75 µg. The same dosage was applied for all subsequent in vivo experiments. The mice that received no treatment served as controls. For intratracheal injection, a 50-µl aliquot of test materials, including algae-NP(DOX)-robot or NP(DOX), was filled into a polytetrafluoroethylene feeding tube, which had been cut to a length of 15 to 20 cm. Subsequently, the feeding tube was gently inserted 0.5 to 1.0 cm into the trachea, and the test material inoculum was administered into the lungs. To prevent leakage of the test materials from the lungs, the feeding tube was kept in place for 30 s. After various time intervals (0, 4, and 24 hours), groups of mice were euthanized, and their lungs were excised for analysis. The fluorescence of the lungs was imaged and quantified using a PerkinElmer Xenogen In Vivo Imaging System (IVIS) 200 system. To measure the remaining amount of DOX, lung tissues were homogenized using a BioSpec Mini-BeadBeater-16. The quantity of DOX was measured using LC-MS, which was performed in the Molecular Mass Spectrometry Facility at UCSD.

To study drug distribution in the lungs, algae-NP(DOX)-robot and NP(DOX) were intratracheally administered to female C57BL/6 mice. At 24 hours after treatment, the lungs were collected and

snap-frozen at -80°C in Tissue-Tek optimal cutting temperature (O.C.T.) compound (Sakura). Cryosections were prepared by the Moores Cancer Center Tissue Technology Shared Resource (Cancer Center Support Grant P30CA23100). To visualize the distribution within the lung tissue, the sections were stained with Hoechst 33342 ($10 \mu\text{g ml}^{-1}$; Thermo Fisher Scientific) at room temperature for 20 min. They were then mounted with Fluoromount-G mounting medium (Invitrogen) and imaged on a Leica SP8 confocal microscope.

In vivo macrophage clearance

After intratracheal injection with algaes-NP(DOX)-robot or NP(DOX), BALF was collected at different time points (1, 4, 8, and 24 hours) following a previously established protocol (29). Briefly, mice were euthanized by CO_2 inhalation, and the trachea was exposed. An incision was made in the trachea, followed by the insertion of a catheter. BALF was obtained through triplicate washes with 0.5 ml of 0.5% (v/v) fetal bovine serum (Gibco) and 2 mM EDTA (Thermo Fisher Scientific) in phosphate-buffered saline (PBS), and the collected samples were stored on ice. The BALF was then centrifuged at 700g for 5 min and treated with RBC lysis buffer (BioLegend) per the manufacturer's instructions. Afterward, the cells were blocked with 1% fetal bovine serum (Gibco) in PBS on ice for 30 min and stained with FITC anti-mouse Siglec-F (S17007L, BioLegend) and Pacific Blue anti-mouse CD11c (N418, BioLegend). After washing with PBS to remove unbound antibodies, cells were resuspended in PBS for flow cytometry analysis. Data were collected using a Becton Dickinson LSR II flow cytometer and analyzed using FlowJo v10.4 software.

In vivo efficacy in a lung metastasis model

To establish an experimental lung metastasis model, 1×10^5 B16-F10-Luc2 cells (ATCC CRL-6475-LUC2) were injected intravenously into the tail vein of female C57BL/6 mice. The mice received treatment with free DOX, NP(DOX), and algaes-NP(DOX)-robot through intratracheal instillation on days 1, 3, 5, and 7 after tumor cell inoculation. Mice without treatment were used as controls. To monitor tumor growth, on days 12, 16, 20, 24, and 28 after tumor cell inoculation, the mice were intraperitoneally administered 200 μl of d-luciferin (5 mg ml^{-1} ; Syd Labs) in Dulbecco's Phosphate-Buffered Saline (DPBS, Gibco). Bioluminescence signals were detected using a PerkinElmer Xenogen IVIS 200 system. The body weight and survival of each mouse were also monitored throughout the study. The survival endpoint was defined as either death or moribundity upon observation.

In vivo safety evaluation

Healthy female C57BL/6 mice were intratracheally administered with free DOX, NP(DOX), and algaes-NP(DOX)-robot every other day for a total of four injections. Mice without treatment were used as controls. At 24 hours following the last treatment, blood samples were collected via submandibular puncture into Microvette 100 EDTA K3E tubes (Sarstedt) for blood cell quantification. To collect serum for comprehensive blood chemistry analysis, blood samples were obtained without any anticoagulant, placed at room temperature for 30 min, and centrifuged at 3000g for 10 min. Both the blood cell quantification and blood chemistry analyses were performed by the Animal Care Program Diagnostic Services Laboratory at UCSD. For histological analysis, the heart, liver, spleen, lungs, and kidneys were

excised and fixed in phosphate-buffered 10% formalin (Fisher Chemical), followed by sectioning and hematoxylin and eosin staining. These histological procedures were conducted by the Moores Cancer Center Tissue Technology Shared Resource.

Statistics and reproducibility

All relevant information is stated in the figure captions. No statistical method was used to predetermine sample size. No data were excluded from the analyses. The investigators were not blinded to allocation during experiments and outcome assessment.

Supplementary Materials

This PDF file includes:

Figs. S1 to S13

Legends for movies S1 to S3

Other Supplementary Material for this manuscript includes the following:

Movies S1 to S3

REFERENCES AND NOTES

- D. X. Nguyen, P. D. Bos, J. Massagué, Metastasis: From dissemination to organ-specific colonization. *Nat. Rev. Cancer* **9**, 274–284 (2009).
- T.-L. H. Mohammed, A. Chowdhry, G. P. Reddy, J. K. Amorosa, K. Brown, D. S. Dyer, M. E. Ginsburg, D. E. Heitkamp, J. Jeudy, J. Kirsch, ACR Appropriateness Criteria® screening for pulmonary metastases. *J. Thorac. Imaging* **26**, W1–W3 (2011).
- N. K. Altorki, G. J. Markowitz, D. Gao, J. L. Port, A. Saxena, B. Stiles, T. McGraw, V. Mittal, The lung microenvironment: An important regulator of tumour growth and metastasis. *Nat. Rev. Cancer* **19**, 9–31 (2019).
- B. A. Chabner, T. G. Roberts Jr., Chemotherapy and the war on cancer. *Nat. Rev. Cancer* **5**, 65–72 (2005).
- S. Azarmi, W. H. Roa, R. Löbenberg, Targeted delivery of nanoparticles for the treatment of lung diseases. *Adv. Drug Deliv. Rev.* **60**, 863–875 (2008).
- A. Schroeder, D. A. Heller, M. M. Winslow, J. E. Dahlman, G. W. Pratt, R. Langer, T. Jacks, D. G. Anderson, Treating metastatic cancer with nanotechnology. *Nat. Rev. Cancer* **12**, 39–50 (2012).
- S. Mitragotri, P. A. Burke, R. Langer, Overcoming the challenges in administering biopharmaceuticals: Formulation and delivery strategies. *Nat. Rev. Drug Discov.* **13**, 655–672 (2014).
- S. Sindhwan, A. M. Syed, J. Ngai, B. R. Kingston, L. Maiorino, J. Rothschild, P. MacMillan, Y. Zhang, N. U. Rajesh, T. Hoang, J. L. Y. Wu, S. Wilhelm, A. Zilman, S. Gadde, A. Sulaiman, B. Ouyang, Z. Lin, L. Wang, M. Egeblad, W. C. W. Chan, The entry of nanoparticles into solid tumours. *Nat. Mater.* **19**, 566–575 (2020).
- E. Blanco, H. Shen, M. Ferrari, Principles of nanoparticle design for overcoming biological barriers to drug delivery. *Nat. Biotechnol.* **33**, 941–951 (2015).
- J. S. Patton, P. R. Byron, Inhaling medicines: Delivering drugs to the body through the lungs. *Nat. Rev. Drug Discov.* **6**, 67–74 (2007).
- H. S. Choi, Y. Ashitake, J. H. Lee, S. H. Kim, A. Matsui, N. Insin, M. G. Bawendi, M. Semmler-Behnke, J. V. Frangioni, A. Tsuda, Rapid translocation of nanoparticles from the lung airspaces to the body. *Nat. Biotechnol.* **28**, 1300–1303 (2010).
- J. S. Patton, Mechanisms of macromolecule absorption by the lungs. *Adv. Drug Deliv. Rev.* **19**, 3–36 (1996).
- O. M. Merkel, M. Zheng, H. Debus, T. Kissel, Pulmonary gene delivery using polymeric nonviral vectors. *Bioconjug. Chem.* **23**, 3–20 (2012).
- C. Loira-Pastoriza, J. Todoroff, R. Vanbever, Delivery strategies for sustained drug release in the lungs. *Adv. Drug Deliv. Rev.* **75**, 81–91 (2014).
- L. Rotolo, D. Vanover, N. C. Bruno, H. E. Peck, C. Zurlo, J. Murray, R. K. Noel, L. O'Farrell, M. Arainga, N. Orr-Burks, J. Y. Joo, L. C. S. Chaves, Y. Jung, J. Beyersdorf, S. Gumber, R. Guerrero-Ferreira, S. Cornejo, M. Thoresen, A. K. Olivier, K. M. Kuo, J. C. Gumbart, A. R. Woolums, F. Villinger, E. R. Lafontaine, R. J. Hogan, M. G. Finn, P. J. Santangelo, Species-agnostic polymeric formulations for inhalable messenger RNA delivery to the lung. *Nat. Mater.* **22**, 369–379 (2023).
- Z. Wang, K. D. Popowski, D. Zhu, B. L. de Juan Abad, X. Wang, M. Liu, H. Lutz, N. De Naeyer, C. T. DeMarco, T. N. Denny, P.-U. C. Dinh, Z. Li, K. Cheng, Exosomes decorated with a recombinant SARS-CoV-2 receptor-binding domain as an inhalable COVID-19 vaccine. *Nat. Biomed. Eng.* **6**, 791–805 (2022).
- P.-U. C. Dinh, D. Paudel, H. Brochu, K. D. Popowski, M. C. Gracieux, J. Cores, K. Huang, M. T. Hensley, E. Harrell, A. C. Vandergriff, Inhalation of lung spheroid cell secretome and exosomes promotes lung repair in pulmonary fibrosis. *Nat. Commun.* **11**, 1064 (2020).

18. Y. Liu, W. N. Crowe, L. Wang, Y. Lu, W. J. Petty, A. A. Habib, D. Zhao, An inhalable nanoparticulate STING agonist synergizes with radiotherapy to confer long-term control of lung metastases. *Nat. Commun.* **10**, 5108 (2019).
19. M. Geiser, W. G. Kreyling, Deposition and biokinetics of inhaled nanoparticles. *Part. Fibre Toxicol.* **7**, 2–17 (2010).
20. J. Li, B. E.-F. de Ávila, W. Gao, L. Zhang, J. Wang, Micro/nanorobots for biomedicine: Delivery, surgery, sensing, and detoxification. *Sci. Robot.* **2**, eaam6431 (2017).
21. B. E.-F. de Ávila, P. Angsantikul, J. Li, M. A. Lopez-Ramirez, D. E. Ramirez-Herrera, S. Thamphiwatana, C. Chen, J. Delezuk, R. Samakapiruk, V. Ramez, M. Obonyo, L. Zhang, J. Wang, Micromotor-enabled active drug delivery for in vivo treatment of stomach infection. *Nat. Commun.* **8**, 272 (2017).
22. H. Zhang, Z. Li, C. Gao, X. Fan, Y. Pang, T. Li, Z. Wu, H. Xie, Q. He, Dual-responsive biohybrid neutrobots for active target delivery. *Sci. Robot.* **6**, aa9519 (2021).
23. M. Wan, Q. Wang, R. Wang, R. Wu, T. Li, D. Fang, Y. Huang, Y. Yu, L. Fang, X. Wang, Y. Zhang, Z. Miao, B. Zhao, F. Wang, C. Mao, Q. Jiang, X. Xu, D. Shi, Platelet-derived porous nanomotor for thrombus therapy. *Sci. Adv.* **6**, eaaz9014 (2020).
24. O. Felfoul, M. Mohammadi, S. Taherkhani, D. De Lanauze, Y. Z. Xu, D. Loghin, S. Essa, S. Jancik, D. Houle, M. Lafleur, L. Gaboury, M. Tabrizian, N. Kaou, M. Atkin, T. Vuong, G. Batist, N. Beauchemin, D. Radzioch, S. Martel, Magneto-aerotactic bacteria deliver drug-containing nanoliposomes to tumour hypoxic regions. *Nat. Nanotechnol.* **11**, 941–947 (2016).
25. Y. Zhang, L. Zhang, L. Yang, C. I. Vong, K. F. Chan, W. K. Wu, T. N. Kwong, N. W. Lo, M. Ip, S. H. Wong, J. J. Y. Sung, P. W. Y. Chiu, L. Zhang, Real-time tracking of fluorescent magnetic spore-based microrobots for remote detection of *C. diff* toxins. *Sci. Adv.* **5**, eaau9650 (2019).
26. Z. Cong, S. Tang, L. Xie, M. Yang, Y. Li, D. Lu, J. Li, Q. Yang, Q. Chen, Z. Zhang, X. Zhang, S. Wu, Magnetic-powered janus cell robots loaded with oncolytic adenovirus for active and targeted virotherapy of bladder cancer. *Adv. Mater.* **34**, e2201042 (2022).
27. M. S. Draz, K. M. Kochehbyoki, A. Vasan, D. Battalapalli, A. Sreeram, M. K. Kanakasabapathy, S. Kallakuri, A. Tsibris, D. R. Kuritzkes, H. Shafiee, DNA engineered micromotors powered by metal nanoparticles for motion based cellphone diagnostics. *Nat. Commun.* **9**, 4282 (2018).
28. C. K. Schmidt, M. Medina-Sánchez, R. J. Edmondson, O. G. Schmidt, Engineering microrobots for targeted cancer therapies from a medical perspective. *Nat. Commun.* **11**, 5618 (2020).
29. F. Zhang, J. Zhuang, Z. Li, H. Gong, B. E.-F. de Ávila, Y. Duan, Q. Zhang, J. Zhou, L. Yin, E. Karshalev, W. Gao, V. Nizet, R. H. Fang, L. Zhang, J. Wang, Nanoparticle-modified microrobots for in vivo antibiotic delivery to treat acute bacterial pneumonia. *Nat. Mater.* **21**, 1324–1332 (2022).
30. S. Palagi, P. Fischer, Bioinspired microrobots. *Nat. Rev. Mater.* **3**, 113–124 (2018).
31. B. Wang, K. F. Chan, K. Yuan, Q. Wang, X. Xia, L. Yang, H. Ko, Y.-X. J. Wang, J. J. Y. Sung, P. W. Y. Chiu, L. Zhang, Endoscopy-assisted magnetic navigation of biohybrid soft microrobots with rapid endoluminal delivery and imaging. *Sci. Robot.* **6**, eabd2813 (2021).
32. P. Wrede, O. Degtyaruk, S. K. Kalva, X. L. Deán-Ben, U. Bozuyuk, A. Aghakhani, B. Akolpoglu, M. Sitti, D. Razansky, Real-time 3D optoacoustic tracking of cell-sized magnetic microrobots circulating in the mouse brain vasculature. *Sci. Adv.* **8**, eabm9132 (2022).
33. Z. Wu, L. Li, Y. Yang, P. Hu, Y. Li, S.-Y. Yang, L. V. Wang, W. Gao, A microrobotic system guided by photoacoustic computed tomography for targeted navigation in intestines in vivo. *Sci. Robot.* **4**, eaax0613 (2019).
34. E. Karshalev, B. Esteban-Fernández de Ávila, M. Beltrán-Gastélum, P. Angsantikul, S. Tang, R. Mundaca-Uribe, F. Zhang, J. Zhao, L. Zhang, J. Wang, Micromotor pills as a dynamic oral delivery platform. *ACS Nano* **12**, 8397–8405 (2018).
35. J. Li, S. Thamphiwatana, W. Liu, B. Esteban-Fernández de Ávila, P. Angsantikul, E. Sandraz, J. Wang, T. Xu, F. Soto, V. Ramez, X. Wang, W. Gao, L. Zhang, J. Wang, Enteric micromotor can selectively position and spontaneously propel in the gastrointestinal tract. *ACS Nano* **10**, 9536–9542 (2016).
36. F. Zhang, Z. Li, Y. Duan, H. Luan, L. Yin, Z. Guo, C. Chen, M. Xu, W. Gao, R. H. Fang, L. Zhang, J. Wang, Extremophile-based biohybrid micromotors for biomedical operations in harsh acidic environments. *Sci. Adv.* **8**, eaade6455 (2022).
37. T. Gwisi, N. Mirkhani, M. G. Christiansen, T. T. Nguyen, V. Ling, S. Schuerle, Magnetic torque-driven living microrobots for increased tumor infiltration. *Sci. Robot.* **7**, eab00665 (2022).
38. D. B. Weibel, P. Garstecki, D. Ryan, W. R. DiLuzio, M. Mayer, J. E. Seto, G. M. Whitesides, Microoxen: Microorganisms to move microscale loads. *Proc. Natl. Acad. Sci. U.S.A.* **102**, 11963–11967 (2005).
39. H. Xu, M. Medina-Sánchez, V. Magdanz, L. Schwarz, F. Hebenstreit, O. G. Schmidt, Sperm-hybrid micromotor for targeted drug delivery. *ACS Nano* **12**, 327–337 (2018).
40. M. B. Akolpoglu, Y. Alapan, N. O. Dogan, S. F. Baltaci, O. Yasa, G. Aybar Tural, M. Sitti, Magnetically steerable bacterial micromotors moving in 3D biological matrices for stimuli-responsive cargo delivery. *Sci. Adv.* **8**, eaab06163 (2022).
41. L. Ricotti, B. Trimmer, A. W. Feinberg, R. Raman, K. K. Parker, R. Bashir, M. Sitti, S. Martel, P. Dario, A. Mencassi, Biohybrid actuators for robotics: A review of devices actuated by living cells. *Sci. Robot.* **2**, eaaoq495 (2017).
42. L. Sun, Y. Yu, Z. Chen, F. Bian, F. Ye, L. Sun, Y. Zhao, Biohybrid robotics with living cell actuation. *Chem. Soc. Rev.* **49**, 4043–4069 (2020).
43. F. Zhang, Z. Li, C. Chen, H. Luan, R. H. Fang, L. Zhang, J. Wang, Biohybrid microalgae robots: Design, fabrication, materials and applications. *Adv. Mater.* **36**, 2303714 (2023).
44. M. B. Akolpoglu, N. O. Dogan, U. Bozuyuk, H. Ceylan, S. Kizilel, M. Sitti, High-yield production of biohybrid microalgae for on-demand cargo delivery. *Adv. Sci.* **16**, 2001256 (2020).
45. I. S. Shchelik, J. V. Molino, K. Gademann, Biohybrid microswimmers against bacterial infections. *Acta Biomater.* **136**, 99–110 (2021).
46. F. Zhang, Z. Li, Y. Duan, A. Abbas, R. Mundaca-Uribe, L. Yin, H. Luan, W. Gao, R. H. Fang, L. Zhang, Gastrointestinal tract drug delivery using algae motors embedded in a degradable capsule. *Sci. Robot.* **7**, eaubo4160 (2022).
47. J. Wang, F. Soto, S. Liu, Q. Yin, E. Purcell, Y. Zeng, E. C. Hsu, D. Akin, B. Sinclair, T. Stoyanova, Voltbots: Volvo microalgae-based robots for multimode precision imaging and therapy. *Adv. Funct. Mater.* **32**, 2201800 (2022).
48. F. Zhang, Z. Li, L. Yin, Q. Zhang, N. Askarinam, R. Mundaca-Uribe, F. Tehrani, E. Karshalev, W. Gao, L. Zhang, ACE2 receptor-modified algae-based microrobot for removal of SARS-CoV-2 in wastewater. *J. Am. Chem. Soc.* **143**, 12194–12201 (2021).
49. Z. Zhao, A. Ukidve, Y. Gao, J. Kim, S. Mitragotri, Erythrocyte leveraged chemotherapy (ELeCt): Nanoparticle assembly on erythrocyte surface to combat lung metastasis. *Sci. Adv.* **5**, eaax9250 (2019).
50. R. H. Fang, A. V. Kroll, W. Gao, L. Zhang, Cell membrane coating nanotechnology. *Adv. Mater.* **30**, 1706759 (2018).
51. T. L. Schenck, U. Hopfner, M. N. Chávez, H.-G. Machens, I. Somlai-Schweiger, R. E. Giunta, A. V. Bohne, J. Nickelsen, M. L. Allende, J. T. Egafña, Photosynthetic biomaterials: A pathway towards autotrophic tissue engineering. *Acta Biomater.* **15**, 39–47 (2015).
52. Y. Ueno, S. Aikawa, A. Kondo, S. Akimoto, Adaptation of light-harvesting functions of unicellular green algae to different light qualities. *Photosynth. Res.* **139**, 145–154 (2019).
53. E. L. Hunter, G. M. Penny, S. K. Dutcher, Algal ciliary motility. *eLS* **2**, <https://doi.org/10.1002/9780470015902.a0029260> (2021).
54. Y. Dong, L. Wang, Z. Zhang, F. Ji, T. K. Chan, H. Yang, C. P. Chan, Z. Yang, Z. Chen, W. T. Chang, J. Y. K. Chan, J. J. Y. Sung, L. Zhang, Endoscope-assisted magnetic helical micromachine delivery for biofilm eradication in tympanostomy tube. *Sci. Adv.* **8**, eabq8573 (2022).
55. A. Del Campo Fonseca, C. Glück, J. Droux, Y. Ferry, C. Frei, S. Wegener, B. Weber, M. El Amki, D. Ahmed, Ultrasound trapping and navigation of microrobots in the mouse brain vasculature. *Nat. Commun.* **14**, 5889 (2023).

Acknowledgments: We are grateful to Y. Su from the Molecular Mass Spectrometry Facility at UCSD for help with LC-MS measurements. **Funding:** This work is supported by the Defense Threat Reduction Agency Joint Science and Technology Office for Chemical and Biological Defense under grant number HDTRA1-21-1-0010 (to L.Z.) and the National Institutes of Health under award number R21AI175904 (to R.H.F.). **Author contributions:** J.W., L.Z., F.Z., Z.G., and Z.L. conceived the idea. F.Z., Z.G., Z.L., R.H.F., L.Z., and J.W. designed the experiments. F.Z., Z.G., Z.L., H.L., Y.Y., and A.T.Z. performed the experiments and collected the data. F.Z., Z.G., Z.L., R.H.F., L.Z., and J.W. drafted the manuscript. All the authors reviewed, edited, and approved the paper. **Competing interests:** The authors declare that they have no competing interests. **Data and materials availability:** All data needed to evaluate the conclusions in the paper are present in the paper and/or the Supplementary Materials.

Submitted 19 December 2023

Accepted 8 May 2024

Published 12 June 2024

10.1126/sciadv.adn6157